# **RESEARCH PAPER**

# Designing g-C<sub>3</sub>N<sub>4</sub>/ZnCo<sub>2</sub>O<sub>4</sub> Modified WO<sub>3</sub> Nanocomposite for Rhodamine Dye Degradation Under Visible Light Irradiation: Synthesis, Characterization, Rational Optimization, and Synergistic Mechanism

Farah S. Khliwi, Hassan A. Alshamsi \*

Department of Chemistry, College of Education, University of Al-Qadisiyah, Diwaniyah, Iraq

### ARTICLE INFO

#### Article History:

Received 21 August 2025 Accepted 23 October 2025 Published 01 January 2026

#### Keywords:

Heterojunction Hydrothermal Photocatalytic degradation Ternary composite ZnCo<sub>2</sub>O<sub>4</sub>

## **ABSTRACT**

In order to develop novel photocatalysts that contribute to the degradation of organic pollutants in water, g-C<sub>3</sub>N<sub>4</sub>/WO<sub>3</sub>/ZnCO<sub>2</sub>O<sub>4</sub> nanocomposite was fabricated using combined ultrasonic and hydrothermal methodologies to create a double Z-scheme system for the degradation of Rhodamine B dye (RhB). The fabricated nanocomposite was first described using various techniques, SEM, XRD, TEM, DRS, EDS, and XPS. XPS and XRD analyses which exhibited the successful distribution of ZnCO2O4 into g-C2N4/ WO<sub>3</sub> nanohybrid and suggest a strong interaction between ZnCO<sub>2</sub>O<sub>4</sub> into g-C<sub>3</sub>N<sub>4</sub>/WO<sub>3</sub>. Microscopic analyses revealed that the ZnCO<sub>2</sub>O<sub>4</sub> into g-C<sub>3</sub>N<sub>4</sub>/ WO<sub>2</sub> nanocomposite have a morphology like lumps with a uniform particle size distribution. Following the characterization, several parameters such as catalyst dosage, pH, and initial pollutant concentration were optimized to achieve best results. Our findings demonstrate that a dual Z-scheme system of g-C<sub>3</sub>N<sub>4</sub>/WO<sub>3</sub>/ZnCO<sub>2</sub>O<sub>4</sub> effectively degrades Rhodamine B. The results showed that the photocatalytic system was able to degrade 98% of rhodamine B within 55 min under the optimal conditions of pH 7 and catalyst dosage of 0.15 g/L. Investigation of various scavengers indicated that that hydroxyl radicals and holes play the most contributing role in the photodegradation of the dye molecules.

## How to cite this article

Khliwi F., Alshamsi H. esigning g- $C_3N_4/ZnCo_2O_4$  Modified  $WO_3$  Nanocomposite for Rhodamine Dye Degradation Under Visible Light Irradiation: Synthesis, Characterization, Rational Optimization, and Synergistic Mechanism. J Nanostruct, 2026; 16(1):141-156. DOI: 10.22052/JNS.2026.01.014

## INTRODUCTION

Water pollution, considered one of the most pressing issues in the world, has occurred due to industrialization and modernization in developing and developed countries. Artificial dyes used in the textile, wood, printing, leather, cosmetics, hygiene, papermaking, and food industries cause various environmental problems after entering the environment due to their toxicity and non-degradability [1]. The health of aquatic organisms

\* Corresponding Author Email: hassan.habeeb@qu.edu.iq

and humans can be at risk due to toxic dyes entering the environment [2]. Azo dyes, which are common and widely used in industry, urgently need to be eliminated because of their chemical stability, non-degradability, and conversion to carcinogenic aromatic species. Reducing the amount of organic pollutants in water and treating industrial wastewater is one of the most difficult challenges for industries and scientific communities. Various methods, such as filtration,

coagulation, and absorption, and in recent years, photocatalytic technology with high degradation efficiency have been used for this purpose [3].

Photocatalytic technology is an advanced oxidation process (AOPs) that is a powerful tool for the degradation of organic pollutants. photocatalytic technology, semiconductor materials called photocatalysts are used for easy, cost-effective, and efficient removal and degradation of organic pollutants [4-6]. Illumination with light energy exceeding the band gap (E<sub>a</sub>) of a semiconductor initiates a phenomenon in which electrons are transferred from the valence band (VB) to the conduction band (CB). This excitation occurs when the valence electrons absorb light energy, allowing them to transfer between bands. This process creates holes (h<sup>+</sup>) in the VB. The resulting electrons and holes act as charge carriers and migrate to the surface of the photocatalyst, where they initiate the redox reaction [7]. The reaction of charge carriers with hydroxyl anions and adsorbed oxygen generates reactive oxygen species (ROS), such as hydroxyl radicals (\*OH) and superoxide radical anions (\*O<sub>2</sub>-), which degrade pollutants [8, 9]. Suitable photocatalysts for photocatalytic applications should have high conductivity, stability, and low electron-hole recombination [10, 11]. To achieve charge transport, nanocomposite materials consisting of several semiconductors with effective band structures can be prepared.

In recent years, as a new and promising photocatalyst, the carbonaceous material graphitic carbon nitride (g-C<sub>3</sub>N<sub>4</sub>), a metal-free π-conjugated semiconductor with a moderate band gap (2.7 eV), has attracted attention because because of its fast charge transport, high thermal conductivity, good light absorption, high specific surface area, and easy and economical synthesis [12]. Studies have shown that hybridization of the C 2p and N 2p orbitals in g-C<sub>3</sub>N<sub>4</sub> leads to the formation of a conduction band (CB), while the valence band (VB) is provided by the N2p orbitals [13]. Nikitha et al. (2024) used synthesized g-C<sub>3</sub>N<sub>4</sub> nanoshells for photocatalytic degradation of crystal violet dye and reported a mineralization of 97% [14]. In a similar report, Wang et al. (2023) used carbondoped g-C<sub>2</sub>N<sub>4</sub> to degrade azo dyes (rhodamine B, amaranth, and methylene blue) and obtained degradation efficiencies ranging from 91.2% to 97.2% [15]. Ganesan et al. (2023) reported 92-95% degradation of azo dyes (methylene blue, methyl orange, and rhodamine B) by thermally exfoliated graphitic carbon nitride [16]. However, the rapid recombination of electron-hole pairs in g-C<sub>3</sub>N<sub>4</sub> and its limited optical response has led to the preparation of composites with other semiconductors. The mechanical and chemical stability of metal oxides has made this class of materials attractive for photocatalytic applications [5]. A review of scientific literature shows that the addition of metal oxides can enhance the degradation of g-C<sub>3</sub>N<sub>4</sub> azo dyes by increasing the number of active sites for redox reactions and generating reactive (radical) species [17]. addition of metal oxides can reduce the band gap energy below 2.7 eV, allowing for better absorption of visible light. Z-pattern photocatalysts, formed by merging several semiconductors and reducing the bandgap energy, increase the efficient separation of electrons and holes in the redox process in the Z-pattern pathway and provide superior redox ability [18]. In Z-pattern heterogeneity, two semiconductors are chosen so that the conduction electrons of one semiconductor can be transferred to the valence band of the other semiconductor. In this case, the potential and ability of two or three semiconductors are fully utilized [19]. Heterojunctions of semiconductors allow for the efficient use of visible light (400-700 nm) for the degradation of organic pollutants, and removal efficiencies of over 99% for organic dyes have been observed with heterojunction photocatalysts [20, 21]. Z-pattern heterojunctions can be used to produce novel photocatalysts for energy production (hydrogen production), water splitting, CO<sub>2</sub> reduction, pollutant degradation, and wastewater treatment [22].

WO<sub>3</sub> nanoparticles have been proven to exhibit photocatalytic activity under visible-light irradiation. In these nanoparticles, the generated charges do not reach the holes at high speeds, so they exhibit excellent photocatalytic activity [23]. The characteristics such as narrow band gap of 2.5-2.8 eV, low electron mobility (cm<sup>2</sup>/Vs), absorption of 12% of the sun light, and hole emission length of about 150 nm make WO, perform better than many other materials [24, 25]. Hkiri et al. (2024) reported more than 98% and 93% removal efficiencies under visible light for methylene blue and Congo red dyes by WO, nanostructures. They concluded that light-generated hydroxyl radicals, hydrogen peroxide, and holes drove the degradation process [26]. Rathod et al. (2024) also showed that WO<sub>3</sub> nanospheres degraded approximately 95% of reactive black 5 (RB5) within 60 min under sunlight. In this case, hydroxyl radicals, as potent oxidizing agents, cause degradation of the dyes [27]. To improve the photocatalytic efficiency of WO<sub>3</sub> nanoparticles, a combination of these nanoparticles with other metal oxides can be used, or dopants such as Mn or Co can be doped [28]. The slower recombination rate of charge carriers generated by visible light irradiation when WO<sub>3</sub> nanoparticles are combined with other metal oxides is the reason byond the increased photodegradation efficiency [29].

Spinel transition metal oxides with the chemical formula AB<sub>2</sub>O<sub>4</sub> have also been considered for photocatalytic applications because of their metal elements with variable valence states and strong activity in alkaline solutions. Spinel oxides with unique optical, magnetic, and electrical properties are economically viable and easily synthesized [30]. ZnCo<sub>2</sub>O<sub>4</sub> is a p-type semiconductor with several advantages, such as biocompatibility, high conductivity, cost-effectiveness, and high theoretical capacitance [31]. The E<sub>g</sub> of this spinel is 2.10 eV, which shows significant absorption of light in the ultraviolet and visible spectrum [32]. At a favorable Co3+/Co2+ ratio, the number of active catalytic sites increases [33]. The exceptional photocatalytic efficacy of ZnCo<sub>2</sub>O<sub>4</sub> for pollutant breakdown is evidenced by its capability to generate hydroxyl and superoxide radicals. ZnCo<sub>2</sub>O<sub>4</sub> has wide applications in electricity generation and storage [34], photocatalytic decomposition [35], and preparation of antimicrobial products [36]. Different photocatalysts based on ZnCo<sub>2</sub>O<sub>4</sub> have been prepared for the photocatalytic degradation of synthetic organic dyes, including ZnCo<sub>2</sub>O<sub>4</sub> [37], and reduced graphene oxide/ZnCo<sub>2</sub>O<sub>4</sub> [31], N-ZnO/ZnCo<sub>2</sub>O<sub>4</sub> [38], nanocomposite ZnCo<sub>2</sub>O<sub>4</sub>/ZnO [39], cation doped ZnO-ZnCo<sub>2</sub>O<sub>4</sub> [40],  $Pd/ZnCo_2O_4$  [30],  $ZnCo_2O_4/CNTs$  [41], and so on. In the present investigation, a nanostructure consisting of a dual Z-scheme heterojunction of ZnCo<sub>2</sub>O<sub>4</sub>, WO<sub>3</sub>, and g-C<sub>3</sub>N<sub>4</sub> was designed to facilitate the transport and separation of charge carriers and enhance the optical properties of Rhodamine B (RhB) dye degradation.

## **MATERIALS AND METHODS**

Synthesis of WO,

For synthesis of tungsten trioxide (WO<sub>3</sub>) nanostructures is via a sol-gel method; initially,

1.5 g of  $\rm Na_2WO_4\cdot 2H_2O$  is dissolved in 100 mL of double-distilled water and stirred for a duration of 10 minutes. The pH of the solution is subsequently adjusted to 1.5 through the addition of 2 M HCl. This mixture is then stirred for 11 hours at room temperature, resulting in the formation of a cloudy precipitate of  $\rm WO_3$ . The precipitate followed by multiple centrifugation cycles and is then dried at 90°C for 2 hours. To enhance the crystallinity of the resulting powders, a heat treatment is performed at 500°C for 2 hours [1].

# Synthesis of $g-C_3N_4$ and $g-C_3N_4/WO_3$

The g-C<sub>3</sub>N<sub>4</sub> was synthesized by using thermal treatment of melamine at 500 °C for three hours and g-C<sub>3</sub>N<sub>4</sub>/WO<sub>3</sub> nanocomposite was prepared via ultrasonication of WO<sub>3</sub> and g-C<sub>3</sub>N<sub>4</sub>. Initially, the g-C<sub>3</sub>N<sub>4</sub> sample underwent sonication for 30 minutes in a mixed solvent composed of ethanol and deionized water, without the addition of WO<sub>3</sub>. Subsequently, the required materials were combined into the initial suspension and agitated for an additional 30 min to achieve different compositions of the g-C<sub>3</sub>N<sub>4</sub>/WO<sub>3</sub> composite. Following sonication, the mixture was allowed to stand to facilitate the sedimentation of the materials. The materials were separated into a centrifuge and then dried in an air oven for 24 hours. Finally, the powders were ground and stored for subsequent characterization and application investigations [42].

# Synthesis of ZnCo<sub>2</sub>O<sub>4</sub> and g-C<sub>3</sub>N<sub>4</sub>/WO<sub>3</sub>/ZnCo<sub>2</sub>O<sub>4</sub>

A straightforward and efficient combustion method is employed for the synthesis of zinc cobalt oxide (ZnCo<sub>3</sub>O<sub>4</sub>) nanoparticles. Initially, 0.01 mol of zinc nitrate hexahydrate (Zn(NO<sub>2</sub>)<sub>2</sub>·6H<sub>2</sub>O) and 0.02 mol of cobalt nitrate hexahydrate (Co(NO<sub>2</sub>)<sub>2</sub>·6H<sub>2</sub>O) are dissolved in 40 mL of double-distilled water. While the solution undergoes vigorous stirring, the temperature is elevated to 85 °C. Subsequently, 6.5 g of citric acid (C<sub>6</sub>H<sub>8</sub>O<sub>7</sub>) is introduced into the solution, and stirring continues for an additional 15 minutes. The resulting solution is then transferred to an oven and heated to 300 °C for 20 minutes. Following this heating process, the resultant powder is ground in a mortar and subsequently annealed for 5 hours at a temperature of 600 °C, utilizing a heating rate of 5 °C/min in an air furnace to yield ZnCo<sub>2</sub>O<sub>4</sub> nanoparticles. The g-C<sub>3</sub>N<sub>4</sub>/WO<sub>3</sub>/ ZnCo<sub>2</sub>O<sub>4</sub> nanocomposite was also synthesized using the same synthesis method of g-C<sub>3</sub>N<sub>4</sub>/WO<sub>3</sub>,

using an ultrasonic probe. In this way, 1 g of the  $g-C_3N_4/WO_3$  nanocomposite and 0.5 g of  $ZnCo_2O_4$  nanoparticles were used to synthesize the  $g-C_3N_4/WO_3/ZnCo_2O_4$  composite [38].

## Characterization of synthesized materials

In this work, characterization approaches were employed to elucidate the ternary composite and its components is included: X-ray diffraction (XRD) analyses that were conducted using a Shimadzu XRD-600 instrument, which utilized CuKα radiation  $(\lambda = 1.54060 \text{ Å})$  at a voltage of 40 kV and a current of 40 mA to identify the crystalline of samples, X-ray photoelectron spectroscopy (XPS) analysis, a Thermo Scientific ESCALAB-250xi, equipped with monochromatic Al Kα radiation at 1486.0 eV. Furthermore, energy-dispersive X-ray spectroscopy (EDS) in conjunction with field emission scanning electron microscopy (FESEM) was employed to investigate the morphology and elemental composition of the samples. A 200 kV accelerating voltage was employed to acquire images utilizing a Philips EM208 instrument. a Perkin Elmer Lambda 365 UV-Vis spectrophotometer was utilized for recording UV-Vis DRS in a wavelength range of 250 nm to 800 nm. For photocatalytic testing, a Shimadzu UV-2550 UV-Vis spectrophotometer was utilized.

## Photocatalytic evaluation

Initially, a 100 mL solution of Rhodamine B (RhB) with a concentration of 15 ppm and natural pH was subjected to magnetic stirring in the presence of 0.01 g of photocatalyst. Before the commencement of photocatalytic degradation, the ability of the catalyst to adsorption of dye molecules was examined in the dark for 30 min under continuous stirring to reach equilibrated adsorption/desorption between catalyst particles and dye molecules. Afterward, the suspensions were then illuminated by a 150 W Xenon arc lamp (ABET technologies) with a UV cutoff filter  $(λ > 420 \text{ nm, light intensity of } 380.8 \text{ μW/cm}^2).$ After 5-minute intervals, 3 mL of the suspension was extracted and centrifuged to separate the photocatalyst. Using UV-Vis spectroscopy the extent of RhB degradation was monitored by measuring the light absorption of the clear liquid

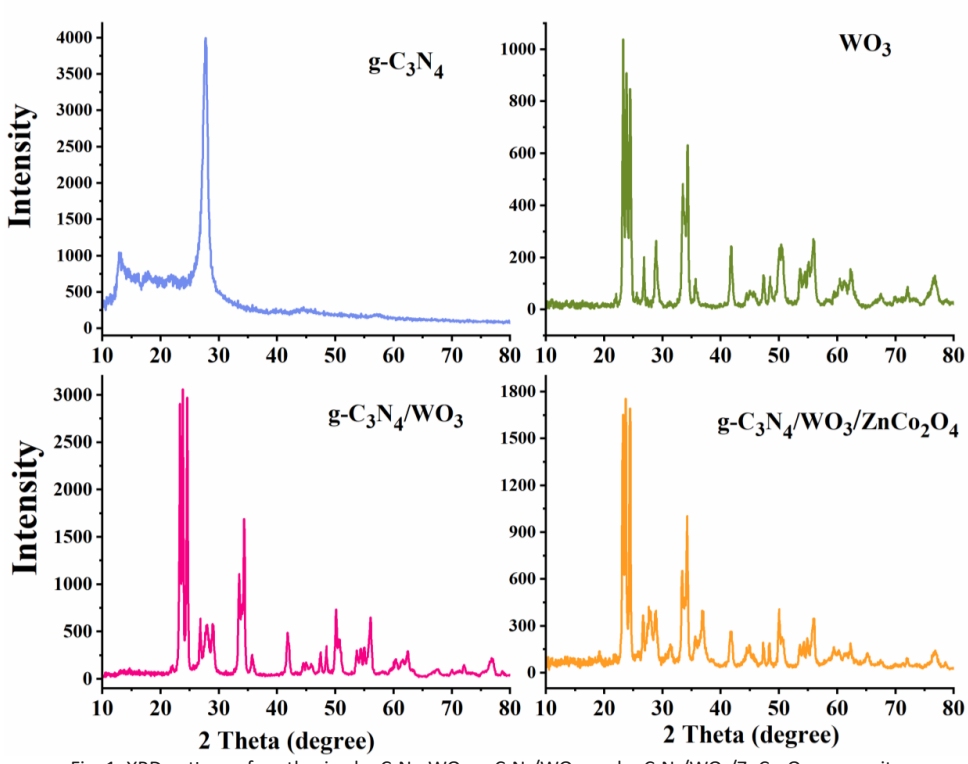


Fig. 1. XRD pattern of synthesized g-C<sub>3</sub>N<sub>4</sub>, WO<sub>3</sub>, g-C<sub>3</sub>N<sub>4</sub>/WO<sub>3</sub>, and g-C<sub>3</sub>N<sub>4</sub>/WO<sub>3</sub>/ZnCo<sub>2</sub>O<sub>4</sub> composite

at  $\lambda$ max of RhB (553 nm). Equation (1) was utilized to calculate the efficiency of photocatalytic degradation reaction.

Photodegradation efficiency (%) =  $((C_0-C_1/C_0))*100 \%$ 

where  $C_0$  repreant the dye concentration at t = 0 and  $C_t$  is the dye concentration at t > 0. The first-order Langmuir-Hinshelwood kinetic model (Equation 2) was adopted to evaluate the kinetics of photocatalytic degradation of the dye.

$$C_t = C_0 e^{-kt}$$

The plot of  $\ln (C_t/C_0)$  versus irradiation time demonstrates a linear relationship. When this relationship is linearized, the resulting slope corresponds to the rate constant (k). The value of the kinetic constant at which the dye

photodegrades indicates how fast the treatment process is occurring.

## **RESULTS AND DISCUSSION**

Characterization study

The structural characterization of the synthesized photocatalysts was performed using X-ray diffraction (XRD). The XRD patterns of  $g\text{-}C_3N_4$ , efficiency  $WO_3$ ,  $g\text{-}C_3N_4/WO_3$ , and  $g\text{-}C_3N_4/WO_3$ /ZnCo $_2O_4$  were systematically analyzed in Fig. 1. In the X-ray diffraction (XRD) pattern of pure  $g\text{-}C_3N_4$ , two peaks were particularly prominent; one peak was observed at 12.89°, while the other was noted at 27.1° that correspond to the (100) and (002) plane reflections, which both observed peaks correspond with the in-plane formation of tri-s-triazine and aromatic species within graphitic carbon nitride. This observation is consistent with the characteristics of layered  $g\text{-}C_3N_4$ , as classified

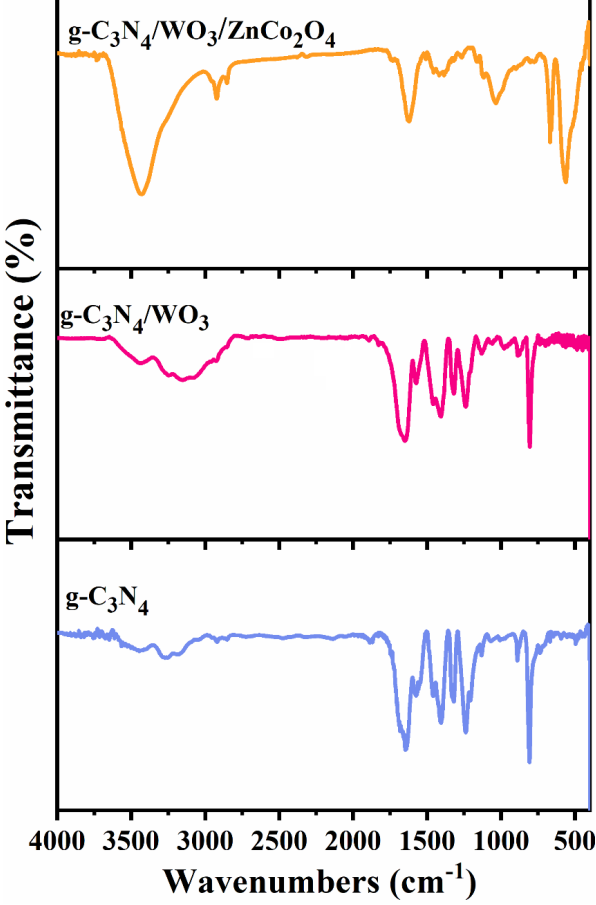


Fig. 2. FT-IR spectra of g-C $_3$ N $_4$ / g-C $_3$ N $_4$ /WO $_3$ , and g-C $_3$ N $_4$ /WO $_3$ /ZnCo $_2$ O $_4$  composite.

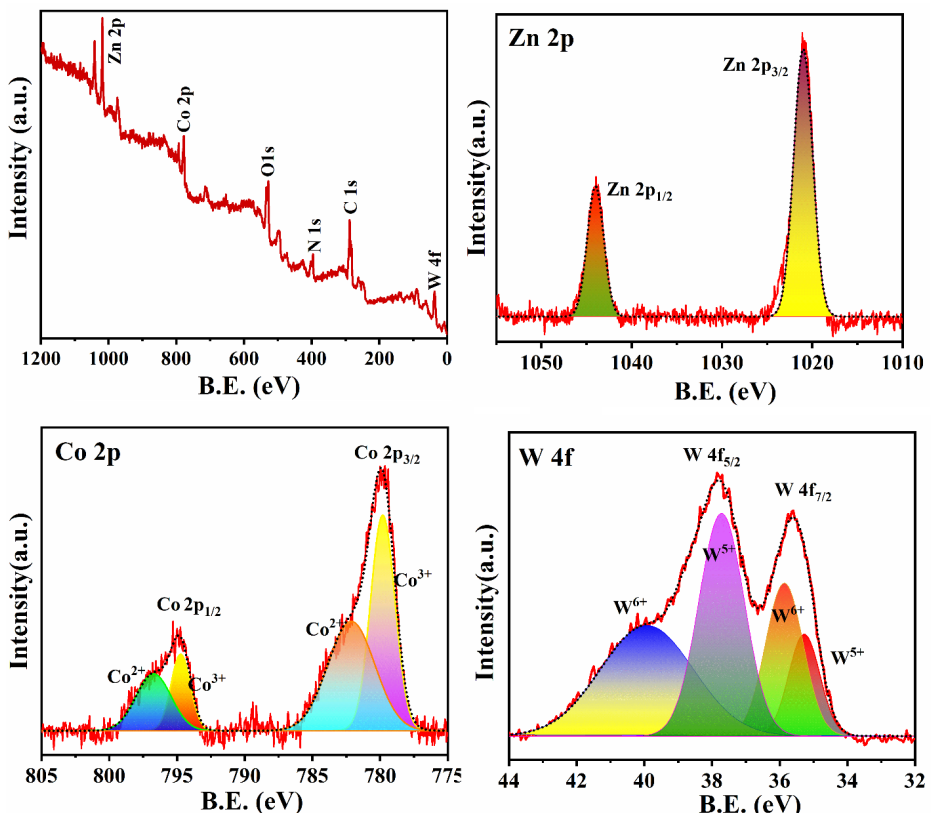
under JCPDS number 87-1526.

The X-Ray diffraction of WO $_3$  exhibits a monoclinic crystal structure (JCPDS 01-072-0677). It is evident that the intensities of the diffraction peaks of g-C $_3$ N $_4$  diminish in the g-C $_3$ N $_4$ /WO $_3$  nanocomposite in Fig. 1. All peaks corresponding to g-C $_3$ N $_4$  and WO $_3$  are depicted in the XRD pattern of the g-C $_3$ N $_4$ /WO $_3$  nanocomposite.

The diffraction pattern of  $\rm ZnCo_2O_4$  in XRD pattern of  $\rm g\text{-}C_3N_4/WO_3/ZnCo_2O_4$  nanocomposite reveals peaks at angles of  $\rm 18.89^\circ$ ,  $\rm 31.32^\circ$ ,  $\rm 36.91^\circ$ ,  $\rm 38.53^\circ$ ,  $\rm 44.86^\circ$ ,  $\rm 55.65^\circ$ ,  $\rm 59.36^\circ$ , and  $\rm 65.19^\circ$ , which correspond to the crystal planes (111), (220), (311), (222), (400), (422), (511), and (440), respectively, with a cubic phase (JCPDS 01-23-1390). The XRD analysis indicates a lack of additional phases or impurities within the  $\rm g\text{-}C_3N_4/WO_3/ZnCo_2O_4$  sample, thereby confirming its single-phase. In addition, all peaks corresponding to  $\rm g\text{-}C_3N_4$  and  $\rm WO_3$  are depicted in the XRD pattern of the  $\rm g\text{-}C_3N_4/WO_3/ZnCo_2O_4$  nanocomposite.

FT-IR spectra of g-C<sub>3</sub>N<sub>4</sub>, g-C<sub>3</sub>N<sub>4</sub>/WO<sub>3</sub>, and

g-C<sub>2</sub>N<sub>4</sub>/WO<sub>2</sub>/ZnCo<sub>2</sub>O<sub>4</sub> composites were utilized to investigate their corresponding functional groups (Fig. 2). The distinct absorption peaks observed in the FT-IR spectra of g-C<sub>2</sub>N<sub>4</sub> are attributed to the vibrations of tri-s-triazine units (810.09 cm 1), C-N stretching vibrations (1200-1700 cm-1), heptazine heterocycles (1631, 1413, and 1244 cm-1), and O-H stretching vibrations (3162-3510 cm<sup>-1</sup>). The characteristic peaks of g-C<sub>3</sub>N<sub>4</sub> are readily detectable in the hybrid composites g-C<sub>3</sub>N<sub>4</sub>/ WO3. The stretching vibration of O-H is indicated by the absorption band at 3454.51 cm<sup>-1</sup> in this spectrum, while the bending vibration of O-H corresponds to 1631.78 cm<sup>-1</sup>, which is associated with moisture-laden water. The peak at 580 cm<sup>-1</sup> is attributed to the vibration of the W-O bond, thereby confirming the presence of WO3 on the surface of g-C<sub>3</sub>N<sub>4</sub>. The emergence of two bands at 565 and 670 cm<sup>-1</sup> in the g-C<sub>3</sub>N<sub>4</sub>/WO<sub>3</sub>/ZnCo<sub>2</sub>O<sub>4</sub> composites is ascribed to the stretching vibrations of Co-O and Zn-O in tetrahedral and octahedral complexes, respectively. This observation further



B.E. (eV)
Fig. 3. The XPS survey spectra and high-resolution XPS spectra of Zn 2p, Co 2p, and W 4f of g-C<sub>3</sub>N<sub>4</sub>/WO<sub>3</sub>/ $ZnCo_3O_4$  composite.

substantiates the effective integration of all functional moieties of g-C<sub>3</sub>N<sub>4</sub>, WO<sub>3</sub>, and ZnCo<sub>2</sub>O<sub>4</sub> within the final composites.

The surface chemical states of the prepared materials evaluate by the X-ray photoelectron spectroscopy (XPS) analyses that are presented in Fig. 3. As demonstrated in the wide scan spectrum in Fig. 3a, the presence of elements included zinc (Zn), cobalt (Co), carbon (C), oxygen (O), tungsten (W), and nitrogen (N) was confirmed in the g-C<sub>3</sub>N<sub>4</sub>/ WO<sub>3</sub>/ZnCo<sub>2</sub>O<sub>4</sub> composite, thereby demonstrating the successful formation of the nanocomposite. The C 1s and N 1s core level spectra were analyzed through deconvolution. In the C 1s spectra, shown in survey spectra, two peaks were fitted at binding energies of 284.87 eV and 288.2 eV, corresponding to C-C and N-C=N bonds, typical of standard carbon and carbon atoms within s-triazine species [43]. The N 1s spectra displayed peak fittings at 398.73 eV, attributed to C-N=C bond, respectively, indicating the presence of sp<sup>2</sup> hybridized carbon and ternary nitrogen groups in graphitic carbon nitride, as illustrated in Fig. 3. Furthermore, the O 1s core level spectra displayed in Figure 3a at survey spectra reveal two peaks at 529.75 eV and 531.83 eV, attributed to absorbed oxygen and crystal lattice oxygen, respectively [43].

The symmetric peaks at binding energies of 1023.13 eV and 1045.9 eV correspond to the Zn  $2p_{3/2}$  and  $Zn 2p_{1/2}$  states of  $Zn^{2+}$ , respectively, as shown in Fig. 3. Additionally, the peaks observed at 780.45 eV and 795.56 eV indicate the Co3+ state of cobalt in the ZnCo<sub>2</sub>O<sub>4</sub> compound, aligning with the Co  $2p_{3/2}$  and Co  $2p_{1/2}$  states [44, 45] as represented in Fig. 3.

In the deconvoluted W4f spectra shown in Fig. 3, the peaks at 37.6 eV and 35.6 eV correspond to the characteristic W 4f<sub>7/2</sub> and W 4f<sub>5/2</sub> (W<sup>+6</sup> states),

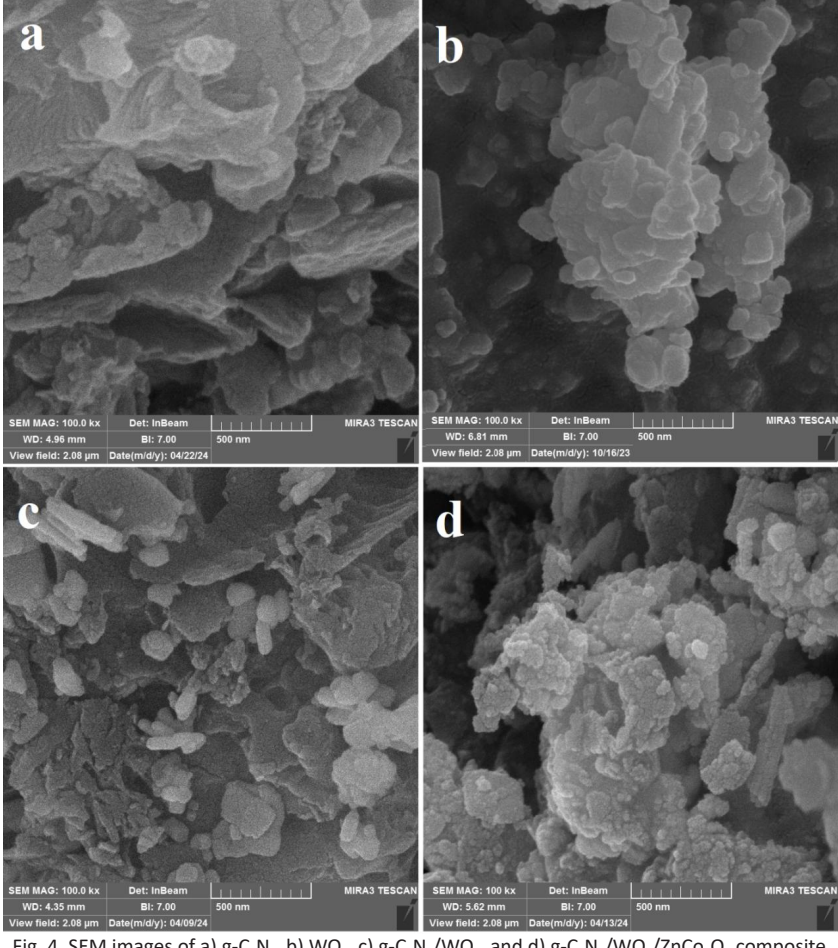


Fig. 4. SEM images of a) g-C<sub>3</sub>N<sub>4</sub>, b) WO<sub>3</sub>, c) g-C<sub>3</sub>N<sub>4</sub>/WO<sub>3</sub>, and d) g-C<sub>3</sub>N<sub>4</sub>/WO<sub>3</sub>/ZnCo<sub>2</sub>O<sub>4</sub> composite.

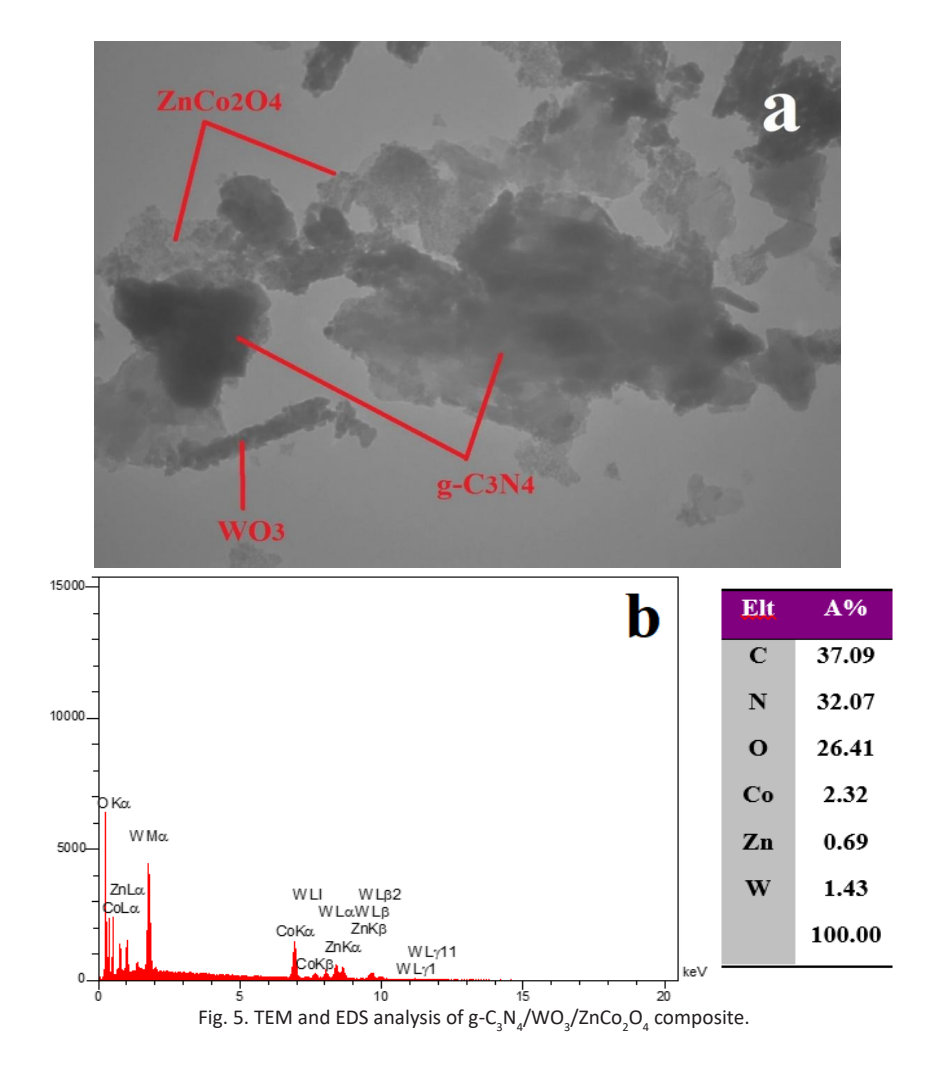
respectively. Meanwhile, the peak at 34.3 eV corresponds to the W<sup>+5</sup> state in WO<sub>2</sub> [42, 46].

Field Emission Scanning Electron Microscopy (FE-SEM) analyses were conducted to investigate the morphological characteristics of the g-C<sub>3</sub>N<sub>4</sub>/WO<sub>3</sub>/ZnCo<sub>2</sub>O<sub>4</sub> composite (Fig. 4). The sheet-like morphology of g-C<sub>3</sub>N<sub>4</sub> and the massive spherical structures alongside short cylindrical structures of WO<sub>3</sub> are observable. Additionally, in the g-C<sub>3</sub>N<sub>4</sub>/WO<sub>3</sub> composite, the plate structures are located next to the short cylinders, which clearly shows the presence of both components. In the g-C<sub>3</sub>N<sub>4</sub>/WO<sub>3</sub>/ZnCo<sub>2</sub>O<sub>4</sub> composite, lumps with a uniform size distribution can be seen, which is expected to improve the photocatalytic properties by increasing the surface area to volume ratio compared to the pure structures.

Another complementary analysis used to

evaluate the morphology of the g-C<sub>3</sub>N<sub>4</sub>/WO<sub>3</sub>/ZnCo<sub>2</sub>O<sub>4</sub> composite was Transmission Electron Microscopy (TEM). In the TEM image (Fig. 5a), the presence of all three components can be clearly seen. In addition, the EDS analysis (Fig. 5b) confirms the XPS analysis results by showing the percentage of C, O, N, Zn, Co, and W elements in an approximate manner and shows that the composite structure was successfully.

The UV-Vis DRS spectra of g- $C_3N_4$ , WO $_3$ , and g- $C_3N_4$ /WO $_3$ /ZnCo $_2O_4$  composite are shown in Fig. 6a. The maximum absorption was observed at approximately 450 nm for the g- $C_3N_4$ /WO $_3$ /ZnCo $_2O_4$  nanocomposite, which displayed significant absorption across the visible light spectrum, while g- $C_3N_4$ and WO $_3$  had a maximum absorption at around 350 nm and 280 nm, respectively. Notably, the presence of ZnCo2O4 induced a redshift in



J Nanostruct 16(1): 141-156, Winter 2026

the maximum absorption at 450 nm. As shown in Fig. 5a, g-C<sub>3</sub>N<sub>4</sub>/WO<sub>3</sub>/ZnCo<sub>3</sub>O<sub>4</sub> exhibited increased visible light absorption relative to the pure g-C<sub>2</sub>N<sub>4</sub> and WO<sub>3</sub> photocatalysts. The incorporation of ZnCo2O4 into the g-C<sub>3</sub>N<sub>4</sub>/WO<sub>3</sub>/ZnCo<sub>3</sub>O<sub>4</sub> heterojunction enhanced its light-harvesting capabilities, resulting in greater absorption in the 380–650 nm range. Furthermore, g-C<sub>3</sub>N<sub>4</sub>/ WO<sub>3</sub>/ZnCo<sub>3</sub>O<sub>4</sub> demonstrated absorption in both the visible and ultraviolet spectra, with higher absorption in the 400-800 nm range compared to the g-C<sub>3</sub>N<sub>4</sub> and WO3 photocatalysts. The band gaps of the synthesized photocatalysts, as depicted in Fig. 6b, were determined using a Tauc plot, revealing that WO<sub>3</sub> and g-C<sub>3</sub>N<sub>4</sub> have nearly identical band gaps of 2.8 eV and 2.4 eV, respectively [47].

Using the Mulliken electronegativity formula,  $E_{CB} = X - Ee - 0.5$  (Eg), the band gap values were used to determine the valence band (VB) and conduction band (CB) edge potentials of g-C<sub>3</sub>N<sub>4</sub> and WO<sub>3</sub> photocatalysts. In this formula,  $E_{CB}$  represents the CB edge potential, X is the geometric mean of the Mulliken electronegativities of the constituent

atoms, Ee is the energy of free electrons on the hydrogen scale ( $\sim$ 4.5 eV), and Eg is the band gap. As shown in Fig. 6b, g-C<sub>3</sub>N<sub>4</sub> and WO<sub>3</sub> photocatalysts were found to have CB values of -0.97 eV and 0.3 eV, respectively, based on the normal hydrogen electrode (NHE) [48]. Similarly, the VB of g-C<sub>3</sub>N<sub>4</sub> and WO<sub>3</sub> photocatalysts were estimated using the empirical formula E<sub>VB</sub> = E<sub>CB</sub> + Eg, which produced values of 1.43 and 3.1 eV. According to the conducted researches, ZnoCo<sub>2</sub>O<sub>4</sub> with a band gap of 2.5 eV has E<sub>VB</sub> and E<sub>CB</sub> level equal to 0.62 and -1.88 eV, respectively.

Synthesized materials were utilized for the photocatalytic degradation of Rhodamine B. Initially, the degradation of Rhodamine B was examined in the presence of light alone; the results indicated that no degradation of Rhodamine B occurred within 75 minutes, and the absorption of RhB remained constant throughout this period. Furthermore, when Rhodamine B was subjected to the g-C<sub>3</sub>N<sub>4</sub>/WO<sub>3</sub>/ZnCo<sub>2</sub>O<sub>4</sub> nanocomposite for 75 minutes, no variation in the absorption of Rhodamine B relative to its initial value was

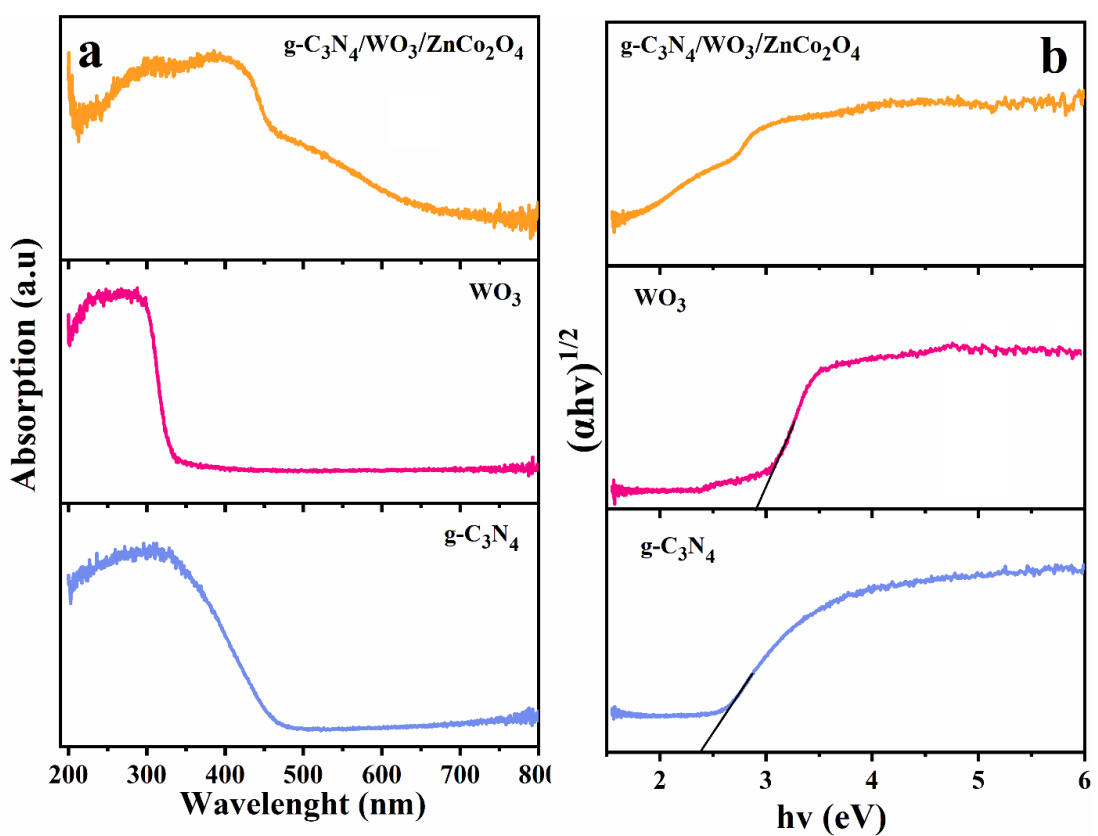


Fig. 6. The a) UV-Vis DRS, b) Tauc plots of g-C<sub>3</sub>N<sub>4</sub> WO<sub>3</sub>, and g-C<sub>3</sub>N<sub>4</sub>/WO<sub>3</sub>/ZnCo<sub>2</sub>O<sub>4</sub> nanocomposite.

observed. Consequently, neither light nor the nanocomposite alone demonstrated any capability to degrade Rhodamine B within 75 minutes.

Subsequently, the degradation of Rhodamine B was analyzed concurrently under light and in conjunction with each of the synthesized materials.

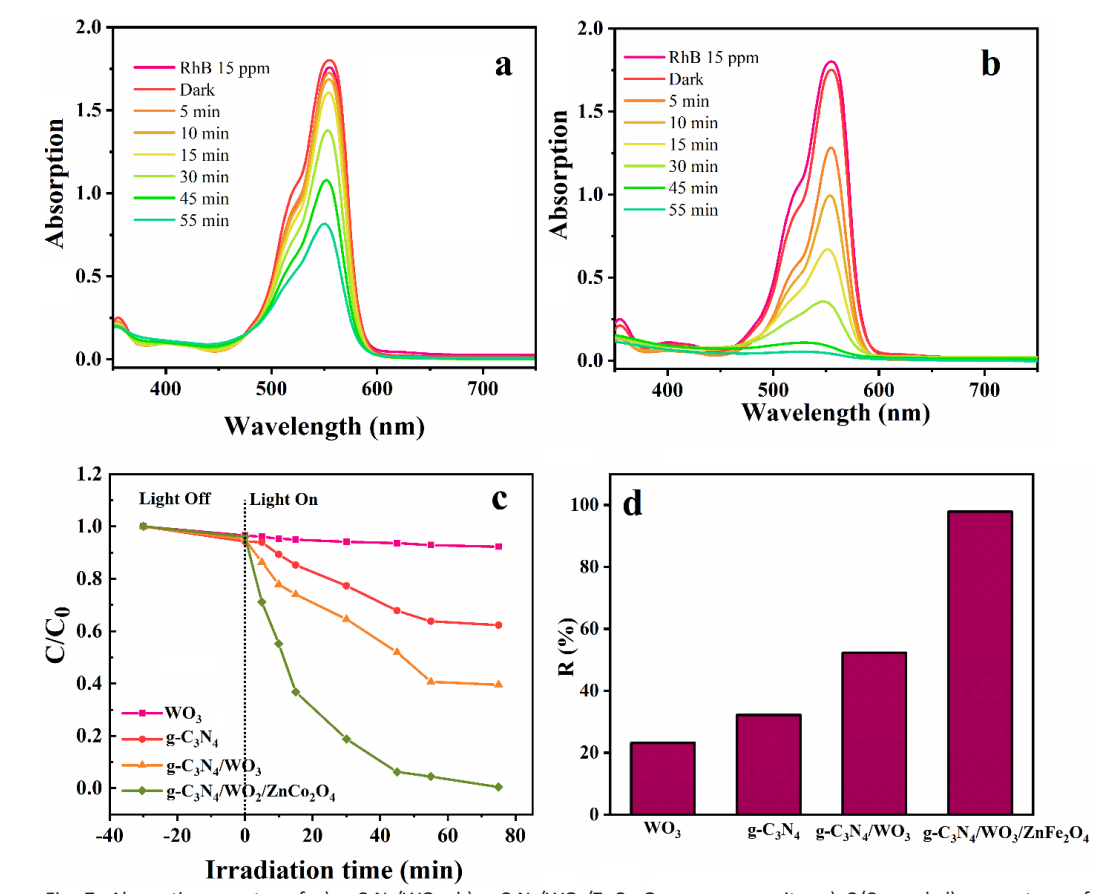


Fig. 7. Absorption spectra of a)  $g-C_3N_4/WO_3$ , b)  $g-C_3N_4/WO_3/ZnCo_2O_4$  nanocomposite, c)  $C/C_0$ , and d) percentage of degradation of RhB in the presence of synthesized nanomaterials.

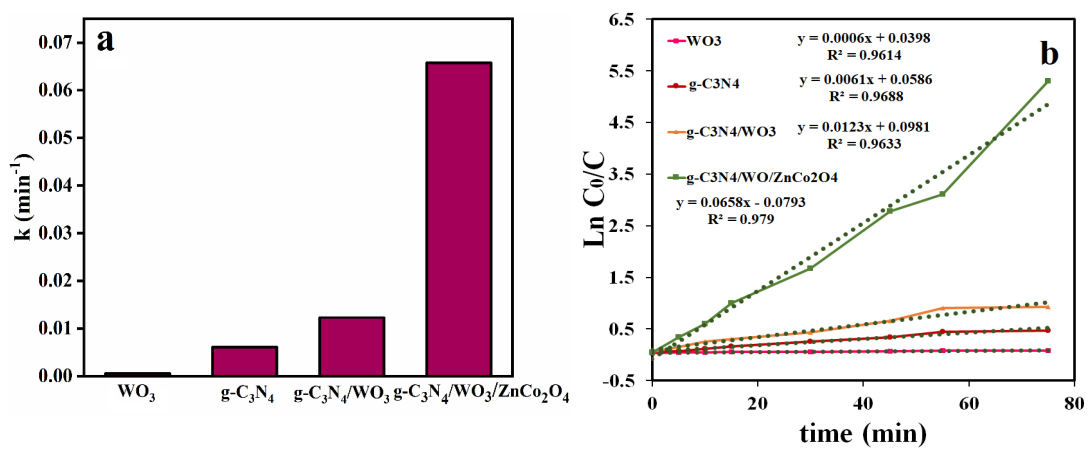


Fig. 8. The kinetic degradation rate constant of Rh.B in the presence of synthesized materials.

The absorption spectra of RhB over 75 minutes in the presence of  $g-C_3N_4/WO_3$ , and the  $g-C_3N_4/WO_3$ /ZnCo<sub>2</sub>O<sub>4</sub> nanocomposite are illustrated in Fig. 7a,b,c. The results revealed that Rhodamine B at pH 7 experienced degradation levels of 23.2 %, 32.1 %, 52.3 %, and 97.9 % in the presence of WO<sub>3</sub>,  $g-C_3N_4$ ,  $g-C_3N_4/WO_3$ , and the  $g-C_3N_4/WO_3$ /ZnCo<sub>2</sub>O<sub>4</sub> nanocomposite, respectively (Fig. 7d), thereby demonstrating the superior performance

of the g-C<sub>3</sub>N<sub>4</sub>/WO<sub>3</sub>/ZnCo<sub>2</sub>O<sub>4</sub> nanocomposite. Fig. 8 displays the rate constants for the photocatalytic degradation of RhB in the presence of the synthesized materials. The rate constants for the photocatalytic degradation of RhB in the presence of WO<sub>3</sub>, g-C<sub>3</sub>N<sub>4</sub>, g-C<sub>3</sub>N<sub>4</sub>/WO<sub>3</sub>, and the g-C<sub>3</sub>N<sub>4</sub>/WO<sub>3</sub>/ZnCo<sub>2</sub>O<sub>4</sub> nanocomposite were determined to be 0.0006 min<sup>-1</sup>, 0.0061 min<sup>-1</sup>, 0.0123 min<sup>-1</sup>, and 0.0658 min<sup>-1</sup>, respectively.

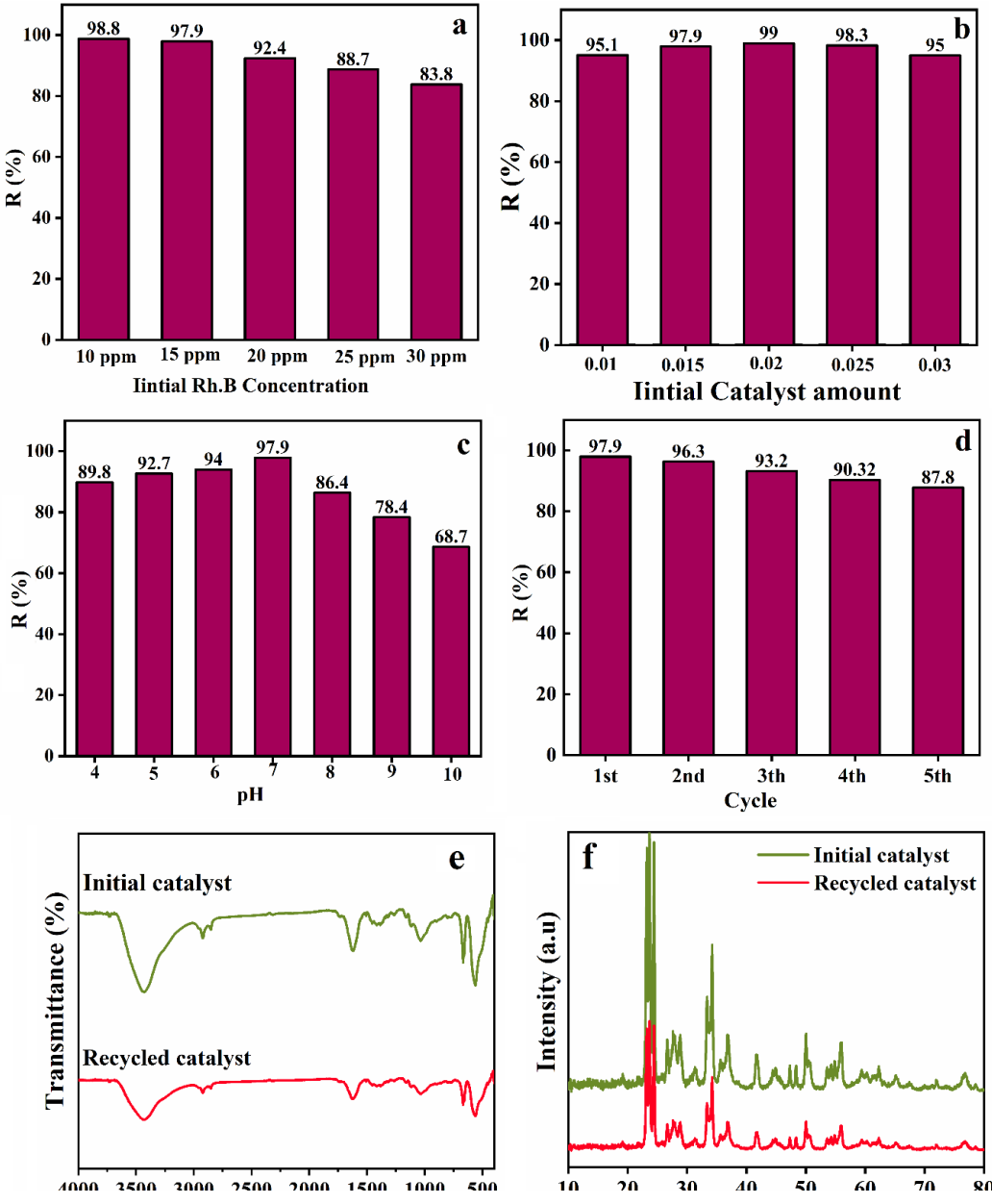


Fig. 9. Investigation of a) Initial RhB concentration, b) Initial catalyst amount, c) pH, d) recyclability, e) FT-IR spectra and f) XRD pattern of g-C<sub>3</sub>N<sub>a</sub>/WO<sub>3</sub>/ZnCo<sub>3</sub>O<sub>4</sub> nanocomposite before and after use.

The enhanced photocatalytic performance of  $g-C_3N_4$  in the presence of  $WO_3$  and  $ZnCo_2O_4$  can be ascribed to a synergistic effect. This synergistic interaction among the synthesized materials results in improved photocatalytic performance, thereby revealing their exceptional degradation capabilities. Notably, the presence of WO<sub>3</sub> and ZnCo<sub>2</sub>O<sub>4</sub> diminishes the bandgap energy, thereby activating the g- $C_3N_4/WO_3/ZnCo_2O_4$  nanocomposite under visible light. Additionally, WO<sub>2</sub> and ZnCo<sub>2</sub>O<sub>4</sub> exhibit substantial surface area and excellent light absorption characteristics, which enhance the generation of electron/hole pairs and facilitate effective photocatalytic reactions in the context of g-C<sub>2</sub>N<sub>4</sub>/WO<sub>2</sub>/ZnCo<sub>2</sub>O<sub>4</sub> owing to their large surface area. Overall, the combination of WO<sub>3</sub> with g-C<sub>3</sub>N<sub>4</sub> and ZnCo<sub>2</sub>O<sub>4</sub> significantly enhances photocatalytic performance and improves efficiency in the degradation of pollutants.

Investigation of Various Parameters in the Photocatalytic Degradation of Rhodamine B

Various parameters that can affect the degradation of RhB were investigated to determine the optimal conditions of dye degradation in the presence of synthesized catalysts. Examining various concentrations of RhB during the photocatalytic degradation process at pH 7 with a dosage of 15 mg in 100 ml RhB 15 ppm is essential. The results show that as the concentration of the RhB increases, the degradation percentage decreases. At higher concentrations, the presence of unadsorbed molecules obstructs light penetration (Fig. 9a).

Additionally, the accumulation of these molecules on the surface of the photocatalyst reduces the amount of light that reaches it, further diminishing the degradation percentage of RhB. To determine the optimum amount of catalyst in the degradation of RhB, various values of catalyst at pH 7 and RhB concentration 15 ppm were used. The absorption spectra obtained showed that by increasing the amount of catalyst from 0.01 g to 0.025 g in the degradation of 100 ml of RhB, the degradation amount increases, but with increasing this amount, due to the accumulation of catalyst on top of each other and also the turbidity of the solution, the light absorption decreases (Fig. 9b).

The photodegradation of RhB process is influenced by pH, and pH is an essential parameter for consideration. Variations in pH have a profound effect on the mechanism of photocatalytic degradation. Consequently, the impact of the initial pH of solution on the photodegradation of RhB was systematically investigated.

The outputs shown that the maximum photodegradation efficiency at a pH of 7, which aligns closely with the natural pH of the RhB solution. In contrast, at a basic pH of around 11, the development of a negative charge on both the catalyst surface and the RhB dye molecules resulted in repulsive interactions, thereby diminishing photodegradation efficiency. Conversely, the use of an acidic solution at approximately pH 4 and 5 led to a slight decrease in catalyst efficiency, attributable to minor dissolution of the catalyst. Consequently, further investigations were conducted without altering the pH of the initial

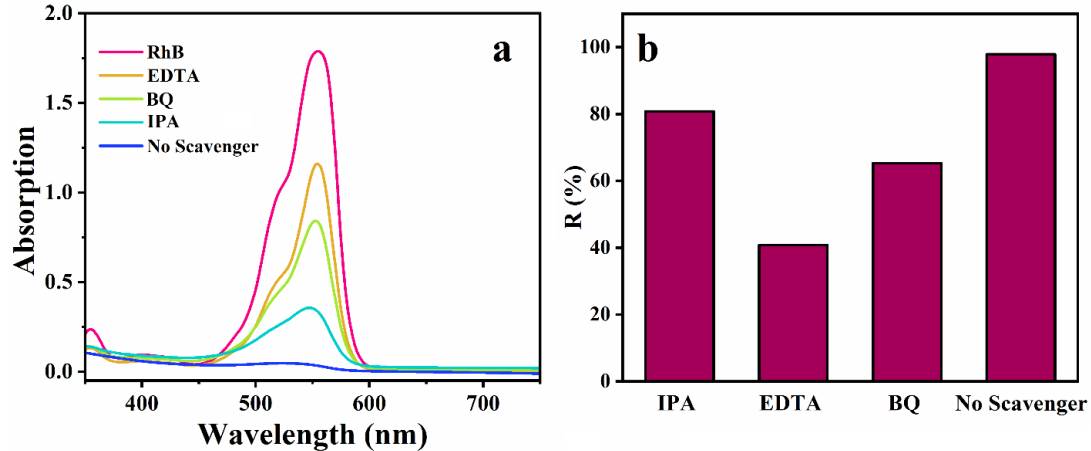


Fig. 10. Photodegradation of  $\widetilde{RhB}$  by  $\widetilde{g}$ - $C_3\widetilde{N_a}/WO_3/ZnCo_2O_4$  nanocomposite in the presence of different scavengers.

solution (Fig. 9c).

The stability of the photocatalitic activity of  $g-C_3N_4/WO_3/ZnCo_2O_4$  nanocomposite was assessed through cyclic experiments, which demonstrated no significant loss in photocatalitic activity after five cycles. These results indicate that the photocatalyst exhibits photostability and can be effectively reused (Fig. 9d).

To prove the stability of the recycled g- $C_3N_4/WO_3/ZnCo_2O_4$  catalysts, FT-IR and XRD analyses were taken, as shown in the Fig. 9e,f. According to the analyses taken, the stability of the catalysts is proven, and this shows that the structure and chemical composition of the catalyst are not degraded after use in successive cycles.

# Photodegradation Mechanism

To investigate the main factor in the degradation of RhB (15 mg/l) in the presence of 15 mg of g-C<sub>3</sub>N<sub>4</sub>/WO<sub>3</sub>/ZnCo<sub>2</sub>O<sub>4</sub> nanocomposite at pH 7, isopropanol alcohol (IPA) as hydroxyl radical scavengers, benzoquinone (BQ) as superoxide scavengers, and EDTA as hole scavengers were used. The findings

showed that when EDTA was present in the degradation process alongside the g-C<sub>3</sub>N<sub>4</sub>/WO<sub>3</sub>/ ZnCo<sub>2</sub>O<sub>4</sub> nanocomposite, the RhB degradation percentage decreased. As illustrated in Fig. 10a, b; following the introduction of IPA, BQ, and EDTA scavengers, the recorded RhB photodegradation were 80.8%, 65.3%, and 40.8%, respectively. In comparison to experiments conducted without scavengers, the removal rates observed with the hydroxyl radical (·OH) and hole (h+) agents were lower, indicating that ·OH and h+ play a critical role in the photocatalytic degradation process. Furthermore, the slight decrease noted in the ·O<sub>2</sub> - experiment suggests that superoxide anion also has a significant impact on photocatalytic degradation of RhB.

A possible mechanism has been proposed based on experimental findings is dual Z-scheme heterojunction for the photocatalytic degradation of RhB. Under visible light irradiation g-C<sub>3</sub>N<sub>4</sub>, WO<sub>3</sub>, and ZnCo<sub>2</sub>O<sub>4</sub> nanostructures are activated, generating photogenerated electron-hole pairs, as illustrated in Fig. 11. The photogenerated holes

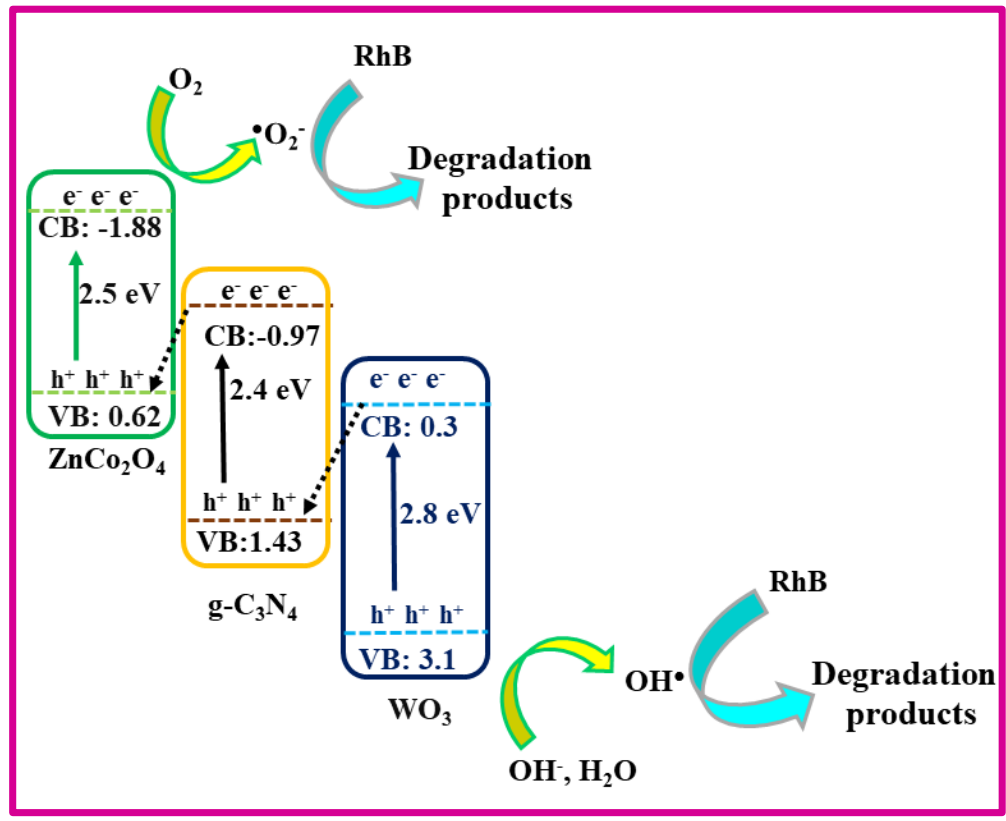


Fig. 11. Possible mechanism of photodegradation of RhB with g-C<sub>2</sub>N<sub>4</sub>/WO<sub>2</sub>/ZnCo<sub>2</sub>O<sub>4</sub> nanocomposite.

remain in the valence band of WO $_3$  nanoparticles, while the electrons in the conduction band are transported to the valence band of g-C $_3$ N $_4$ , where they recombine with holes. Meanwhile, the photogenerated electrons from the valence band of g-C $_3$ N $_4$  migrate to the conduction band (CB) of ZnCo $_3$ O $_4$ .

ZnCo<sub>2</sub>O<sub>4</sub> has a band gap of 2.5 eV, with conduction band and valence band energy levels of -1.88 eV and 0.62 eV, respectively. Consequently, the photogenerated holes in the valence band of ZnCo<sub>2</sub>O<sub>4</sub> do not directly contribute to the degradation of the RhB, as they recombine with electrons transferred from the valence band of g-C<sub>2</sub>N<sub>4</sub>. This recombination occurs mainly because the energy level of the photogenerated holes is 0.62 eV lower than the reaction potential energy of (E (OH $^-$ / $^{\circ}$ OH) = 1.99 eV). In contrast, the photogenerated holes in the conduction band of WO<sub>3</sub> react with OH<sup>-</sup> to produce hydroxyl radicals (•OH), which significantly contribute to the degradation of Rh.B. Additionally, the electrons in the conduction band of ZnCo2O4 are captured by adsorbed O2, resulting in the formation of superoxide anions ( ${}^{\bullet}O_{3}^{-}$ ).

The degradation mechanism indicates that the primary active species are holes (h+) and hydroxyl radicals (•OH), rather than superoxide anions, which aligns with the results of scavenger tests.

## CONCLUSION

The design of a dual Z-scheme heterojunction of g-C<sub>2</sub>N<sub>4</sub>/WO<sub>3</sub>/ZnCo<sub>2</sub>O<sub>4</sub> nanocomposite is attributed to the improved charge transfer of the synthesized nanocomposite compared to the individual components of the synthesized nanocomposite. The g-C<sub>3</sub>N<sub>4</sub> acts as a charge carrier and facilitates electron transfer between WO<sub>3</sub> and ZnCo<sub>2</sub>O<sub>4</sub>, which leads to reduced electron recombination and increased photocatalytic efficiency. On the other hand, the presence of ZnCo<sub>2</sub>O<sub>4</sub> with a large surface area enhances the pollutant loading on the surface of the synthesized nanocomposite, resulting in increased degradation of pollutants. The g-C<sub>2</sub>N<sub>4</sub>/WO<sub>3</sub>/ZnCo<sub>2</sub>O<sub>4</sub> nanocomposite, due to its suitable bandgap energy, is activated under visible light, enhancing the overall photocatalytic activity of the system and allowing for greater pollutant adsorption, leading to more degradation. The maximum degradation efficiency of the g-C<sub>2</sub>N<sub>4</sub>/ WO<sub>3</sub>/ZnCo<sub>3</sub>O<sub>4</sub> composite was around 98% when the optimal condition of 15 mg of catalyst was used

at pH 7 and at ambient temperature, highlighting its potential as an effective photocatalyst for organic dye degradation, especially in industrial textile applications.

#### **ACKNOWLEDGMENTS**

The authors are grateful to University of the Al Qadisiyah, College of Education for their support.

## **CONFLICT OF INTEREST**

The authors declare that there is no conflict of interests regarding the publication of this manuscript.

#### REFERENCES

- Rubesh Ashok Kumar S, Vasvini Mary D, Suganya Josephine GA, Sivasamy A. Hydrothermally synthesized WO<sub>3</sub>:CeO<sub>2</sub> supported gC<sub>3</sub>N<sub>4</sub> nanolayers for rapid photocatalytic degradation of azo dye under natural sunlight. Inorg Chem Commun. 2024;164:112366.
- Parasuraman B, Ganapathi B, Kandasamy B, Ganesan M, Thangavelu P. Fabrication of g-C<sub>3</sub>N<sub>4</sub> nanosheet anchored NiZn<sub>2</sub>O<sub>4</sub> nanocomposites for enhanced photocatalytic dye degradation. Chem Phys Lett. 2024;842:141206.
- Guo Y, Li C, Gong Z, Guo Y, Wang X, Gao B, et al. Photocatalytic decontamination of tetracycline and Cr(VI) by a novel α-FeOOH/FeS<sub>2</sub> photocatalyst: One-pot hydrothermal synthesis and Z-scheme reaction mechanism insight. J Hazard Mater. 2020;397:122580.
- Milad Tabatabaeinejad S, Yousif QA, Abbas Alshamsi H, Al-Nayili A, Salavati-Niasari M. Ultrasound-assisted fabrication and characterization of a novel UV-light-responsive Er<sub>2</sub>Cu<sub>2</sub>O<sub>5</sub> semiconductor nanoparticle Photocatalyst. Arabian Journal of Chemistry. 2022;15(6):103826.
- Al-Nayili A, Alhaidry WA. Novel surface structure of LaFeO<sub>3</sub>/ nitrogen-deficient g-C<sub>3</sub>N<sub>4</sub> nanocomposites to improve visible-light photocatalytic performance toward phenol removal. Environmental Science and Pollution Research. 2024;31(6):8781-8797.
- Dayekh NS, Al-Nayili A. Heterogeneous photocatalytic degradation of phenol over Pd/rGO sheets. AIP Conference Proceedings: AIP Publishing; 2022. p. 030010.
- Abbas Alshamsi H, Abbas. Al Bedairy M, Hussein Alwan S. Visible light assisted photocatalytic degradation of Rhodamine B dye on CdSe-ZnO nanocomposite: Characterization and kinetic studies. IOP Conference Series: Earth and Environmental Science. 2021;722(1):012005.
- Saxena V, Bhagat N, Choudhury S, Mahajan A, Singh A. Phase Variation of Ultrathin WO<sub>3</sub> Electron-Transport Layer Prepared by Scalable Langmuir–Blodgett Technique to Boost Efficiency of Dye Sensitized Solar Cells. Solar RRL. 2022;6(8).
- 9. Al-Nayili A, Haimd SA. Design of a New  $\rm ZnCo_2O_4$  Nanoparticles/Nitrogen-Rich  $\rm g-C_3N_4$  Sheet with Improved Photocatalytic Activity Under Visible Light. J Cluster Sci. 2023;35(1):341-358.
- Zhang Y, Zhang C, Shao D, Xu H, Rao Y, Tan G, et al. Magnetically assembled electrodes based on Pt, RuO<sub>2</sub>-IrO<sub>2</sub>-TiO<sub>2</sub> and Sb-SnO<sub>2</sub> for electrochemical oxidation of

- wastewater featured by fluctuant Cl- concentration. J Hazard Mater. 2022;421:126803.
- Al-nayili A, Alhaidry WA. Perovskite LaFeO<sub>3</sub>/Nitrogen-Deficient G-C<sub>3</sub>N<sub>4</sub> Nanocomposites: Synthesis, Interface Characteristics and Enhanced Photocatalytic Activity. Elsevier BV: 2023.
- Hamza A, Alshamsi H. Novel Z-Scheme g-C<sub>3</sub>N<sub>4</sub>/TiO<sub>2</sub>/NiCo<sub>2</sub>O<sub>4</sub>
  Heterojunctions for Efficient Photocatalytic Degradation of
  Rhodamine B under Visible Light Irradiation. J Cluster Sci.
  2024;35(7):2539-2556.
- 13. Zhang X, Xu B, Li X, Fan X, Zhang J, Yu Y, et al. Anaerobic environment-induced efficient degradation of chloroquine phosphate: Insights into the role of metal-free C<sub>3</sub>N<sub>4</sub> nanotube in visible light-driven peroxymonosulfate activation. Chem Eng J. 2023;457:141219.
- Kim J, Mayorga-Burrezo P, Song S-J, Mayorga-Martinez CC, Medina-Sánchez M, Pané S, et al. Advanced materials for micro/nanorobotics. Chem Soc Rev. 2024;53(18):9190-9253.
- 15. Wang S, Yang J, Cong H, Li X, Wang R, Yang M, et al. C-Doped g-  $C_3N_4$  for Enhanced Photocatalytic Degradation of Azo Dyes under Visible Light. ChemistrySelect. 2023;8(45).
- 16. Ganesan S, Kokulnathan T, Sumathi S, Palaniappan A. Efficient photocatalytic degradation of textile dye pollutants using thermally exfoliated graphitic carbon nitride (TE–g–C<sub>2</sub>N<sub>a</sub>). Sci Rep. 2024;14(1).
- Wang Y, Yang W, Ding K. Synergistic Ag/g-C<sub>3</sub>N<sub>4</sub> H<sub>2</sub>O<sub>2</sub> System for Photocatalytic Degradation of Azo Dyes. Molecules. 2024;29(16):3871.
- 18. Hamza AM, Alshamsi HA. Design of novel Z-scheme g-C<sub>3</sub>N<sub>a</sub>/TiO<sub>2</sub>/CuCo<sub>2</sub>O<sub>4</sub> heterojunctions for efficient visible light-driven photocatalyic degradation of Rhodamine B. Springer Science and Business Media LLC; 2024. http://dx.doi.org/10.21203/rs.3.rs-4566196/v1
- Khliwi FS, Alshamsi HA. Design of a Z-Scheme System with g-C<sub>3</sub>N<sub>4</sub>/WO<sub>3</sub>/ZnFe<sub>2</sub>O<sub>4</sub> Nanocomposite for Photocatalytic Degradation of Rhodamine B. J Cluster Sci. 2025;36(3).
- Yu T, Wang D, Li L, Song W, Pang X, Liang C. A Novel Organic/ Inorganic Dual Z-Scheme Photocatalyst with Visible-Light Response for Organic Pollutants Degradation. Catalysts. 2023;13(11):1391.
- Abkar E, Al-Nayili A, Amiri O, Ghanbari M, Salavati-Niasari M. Facile sonochemical method for preparation of Cs<sub>2</sub>Hgl<sub>4</sub> nanostructures as a promising visible-light photocatalyst. Ultrason Sonochem. 2021;80:105827.
- Albusalih RH, Alshamsi HA. Enhancement of Photocatalytic Degradation of RhB Dye Using CuWO<sub>4</sub>/ZnO/N-g-C<sub>3</sub>N<sub>4</sub> Nanocomposite Under Visible Light Irradiation. J Cluster Sci. 2025;36(4).
- Suhan MBK, Shuchi SB, Al-Mamun MR, Roy H, Islam MS. Enhanced UV light-driven photocatalytic degradation of methyl orange using MoO<sub>3</sub>/WO<sub>3</sub>-fluorinated TiO<sub>2</sub> nanocomposites. Environmental Nanotechnology, Monitoring & Damp; Management. 2023;19:100768.
- Huang ZF, Song J, Pan L, Zhang X, Wang L, Zou JJ. Tungsten Oxides for Photocatalysis, Electrochemistry, and Phototherapy. Adv Mater. 2015;27(36):5309-5327.
- 25. Mi Q, Zhanaidarova A, Brunschwig BS, Gray HB, Lewis NS. A quantitative assessment of the competition between water and anion oxidation at WO<sub>3</sub> photoanodes in acidic aqueous electrolytes. Energy and Environmental Science. 2012;5(2):5694.
- 26. Hkiri K, Mohamed HEA, Harrisankar N, Gibaud A, van

- Steen E, Maaza M. Environmental water treatment with green synthesized  $WO_3$  nanoflakes for cationic and anionic dyes removal: Photocatalytic studies. Catal Commun. 2024;187:106851.
- Rathod S, Pataniya P, Joshi KK, Shekh M, Sumesh CK, Kapatel S. Synergistic RB5 dye degradation and oxygen evolution reaction (OER) catalysis by WO<sub>3</sub> nano-pellets: mechanistic insights and water remediation applications. Surfaces and Interfaces. 2024;48:104216.
- Montazerghaem L, Keramatifarhodbonab M, Naeimi A. Photocatalytic degradation of acid blue 74 by Co: WO<sub>3</sub> nanoparticles: Kinetics and response surface methodology studies. Heliyon. 2024;10(3):e24789.
- Ajel MK, Al-nayili A. Synthesis, characterization of Ag-WO<sub>3</sub>/bentonite nanocomposites and their application in photocatalytic degradation of humic acid in water. Environmental Science and Pollution Research. 2022;30(8):20775-20789.
- Nasir KH, Alshamsi HA. Photocatalytic Degradation of Rhodamine B Using ZnCo<sub>2</sub>O<sub>4</sub>/N-doped g-C<sub>3</sub>N<sub>4</sub> Nanocomposite. Journal of Inorganic and Organometallic Polymers and Materials. 2024;34(12):5925-5942.
- 31. Jiang R, Wang S, Du M, Zhang L, Cao J, Zeng Y, et al. Temperature-dependent formaldehyde and xylene dual selectivity in ZnCo<sub>2</sub>O<sub>4</sub> sphere-like architectures. Colloids Surf Physicochem Eng Aspects. 2023;675:132042.
- Pan H, Wang F, Huang J, Chen N. Binding Characteristics of CoPc/SnO<sub>2</sub> by In-situ Process and Photocatalytic Activity under Visible Light Irradiation. Acta Physico-Chimica Sinica. 2008;24(6):992-996.
- Arulprakash G, Kareem A, Sellappan S, R V. Engineering the morphology of ZnCo2O4 through different synthetic approaches for enhanced OER performance. Int J Hydrogen Energy. 2024;66:625-635.
- 34. Han MC, Zou Mc, Yi TF, Wei F. Recent Advances of ZnCo<sub>2</sub>O<sub>4</sub>-based Anode Materials for Li-ion Batteries. Chemistry An Asian Journal. 2022;18(1).
- Khaled I, Bagtache R, Kadri M, Chergui A, Trari M. Physical and photo-electrochemical properties of the hetero-junction ZnCo2O4/ZnO prepared by nitrate route: Application to photodegradation of Indigo Carmine. Inorg Chem Commun. 2024;159:111818.
- 36. Zhou T, Sun J, Wang K, Gao H, Lv M, Si T, et al. Construction of a highly reactive Zn/NiCo<sub>2</sub>O<sub>4</sub> surface and analysis of its antimicrobial properties. Vacuum. 2024;221:112943.
- 37. Hemamalini S, Manimekalai R. Synthesis, physicochemical and photocatalytic activities of nano ZnCo<sub>2</sub>O<sub>4</sub> catalyst for photodegradation of various dyes under sunlight irradiation. Bull Mater Sci. 2021;44(2).
- Manikandan V, Gayathri R, Zeenath MA. Facile synthesis of rGO/ZnCo<sub>2</sub>O<sub>4</sub> nanocomposite for enhanced photocatalytic dye degradation of crystal violet dye solution. Nano-Structures & Dipole Structures & Dipole Str
- Ebrahimifar M, Kazeminezhad I, Rahimi A. In situ hydrothermal synthesis of ZnCo<sub>2</sub>O<sub>4</sub>/ZnO nanocomposite: Structural, optical, electrochemical properties and photocatalytic performance under visible light. Optik. 2024;312:171976.
- 40. Goswami K, Ananthakrishnan R, Mandal S. Facile synthesis of cation doped ZnO- ZnCo<sub>2</sub>O<sub>4</sub> hetero-nanocomposites for photocatalytic decomposition of aqueous organics under visible light. Materials Chemistry and Physics. 2018;206:174-185.

- 41. Wang J, Wang G, Wang S, Hao J, Liu B. Preparation of ZnCo<sub>2</sub>O<sub>4</sub> Nanosheets Coated on evenly arranged and fully separated Nanowires with high capacitive and photocatalytic properties by a One-Step Low-Temperature Water bath method. ChemistrySelect. 2022;7(13).
- 42. Ibrahim YO, Gondal MA. Visible-light-driven photocatalytic performance of a Z-scheme based TiO<sub>2</sub>/WO<sub>3</sub>/g-C<sub>3</sub>N<sub>4</sub> ternary heterojunctions. Molecular Catalysis. 2021;505:111494.
- 43. Roshan Chandrapal R, Bakiyaraj G, Bharathkumar S, Ganesh V, Archana J, Navaneethan M. Novel combustion technique synthesis of ZnCo<sub>2</sub>O<sub>4</sub> nanobeads/g-C<sub>3</sub>N<sub>4</sub> nanosheet heterojunction photocatalyst in-effect of enhancing photocatalytic degradation for environmental remediation. Surfaces and Interfaces. 2023;41:103269.
- 44. Vijayanand S, Joy PA, Potdar HS, Patil D, Patil P. Nanostructured spinel ZnCo<sub>2</sub>O<sub>4</sub> for the detection of LPG.

- Sensors Actuators B: Chem. 2011;152(1):121-129.
- 45. Kim TW, Woo MA, Regis M, Choi K-S. Electrochemical Synthesis of Spinel Type ZnCo<sub>2</sub>O<sub>4</sub> Electrodes for Use as Oxygen Evolution Reaction Catalysts. The Journal of Physical Chemistry Letters. 2014;5(13):2370-2374.
- Pan JH, Lee WI. Preparation of Highly Ordered Cubic Mesoporous WO<sub>3</sub>/TiO<sub>2</sub> Films and Their Photocatalytic Properties. Chem Mater. 2006;18(3):847-853.
- 47. Tian M, Hu C, Yu J, Chen L. Carbon quantum dots (CQDs) mediated Z-scheme g–C<sub>3</sub>N<sub>4</sub>–CQDs/BiVO<sub>4</sub> heterojunction with enhanced visible light photocatalytic degradation of Paraben. Chemosphere. 2023;323:138248.
- 48. Xia Y, Xiao J, Zhang J, Huang R, Huang X, Yan G, et al. Construction of a sunflower-like S-scheme WO3/ZnIn2S4 heterojunction with spatial charge transfer for enhanced photocatalytic CO, reduction. Fuel. 2025;382:133779.